

# Density Changes in Low Pressure Gas Targets for Electron Scattering Experiments

S. N. Santiesteban<sup>a</sup>, S. Alsalmi<sup>b</sup>, D. Meekins<sup>c</sup>, C. Ayerbe Gayoso<sup>e</sup>, J. Bane<sup>d</sup>,  
S. Barcus<sup>e</sup>, J. Campbell<sup>f</sup>, J. Castellanos<sup>g</sup>, R. Cruz-Torres<sup>h</sup>, H. Dai<sup>i</sup>,  
T. Hague<sup>b</sup>, F. Hauenstein<sup>j</sup>, D. W. Higinbotham<sup>c,\*</sup>, R. J. Holt<sup>l,k</sup>, T. Kutz<sup>n</sup>,  
S. Li<sup>a</sup>, H. Liu<sup>m</sup>, R. E. McClellan<sup>c</sup>, M. Nycz<sup>b</sup>, D. Nguyen<sup>o</sup>, B. Pandey<sup>p</sup>,  
V. Pandey<sup>i</sup>, A. Schmidt<sup>h</sup>, T. Su<sup>b</sup>, Z. Ye<sup>l</sup>

<sup>a</sup>University of New Hampshire, Durham, New Hampshire 03824, USA

<sup>b</sup>Kent State University, Kent, Ohio 44240, USA

<sup>c</sup>Jefferson Lab, Newport News, Virginia 23601 USA

<sup>d</sup>The University of Tennessee, Knoxville, Tennessee 37996, USA

<sup>e</sup>The College of William and Mary, Williamsburg, Virginia 23187, USA

<sup>f</sup>Saint Mary's University, Halifax, Nova Scotia, Canada

<sup>g</sup>Florida International University, Miami, Florida 33199 USA

<sup>h</sup>Massachusetts Institute of Technology, Cambridge, Massachusetts 02139, USA

<sup>i</sup>Center for Neutrino Physics, Virginia Tech, Blacksburg, Virginia 24061, USA

<sup>j</sup>Old Dominion University, Norfolk, Virginia 23529, USA

<sup>k</sup>Kellogg Radiation Laboratory, California Institute of Technology, Pasadena California  
91125 USA

<sup>l</sup>Physics Division, Argonne National Laboratory, Argonne, Illinois 60439, USA

<sup>m</sup>Columbia University, New York, New York 10027, USA

<sup>n</sup>Stony Brook University, Stony Brook, New York 11794, USA

<sup>o</sup>Department of Physics, University of Virginia, Charlottesville, Virginia 22904, USA

<sup>p</sup>Hampton University, Hampton, Virginia 23669, USA

---

## Abstract

A system of modular sealed gas target cells has been developed for use in electron scattering experiments at the Thomas Jefferson National Accelerator Facility (Jefferson Lab). This system was initially developed to complete the MARATHON experiment which required, among other species, tritium as a target material. The system has been used in several of the 12 GeV era experiments in Experimental Hall A using the Jefferson Lab Continuous Electron Beam Accelerator Facility (CEBAF). Thus far, the cells have been loaded with the gas species  $^3\text{H}$ ,  $^3\text{He}$ ,  $^2\text{H}$ ,  $^1\text{H}$  and  $^{40}\text{Ar}$  and operated in nominal beam currents of up to  $22.5\ \mu\text{A}$ . While the gas density of the cells at the time of loading is known, the density of each gas varies uniquely when heated by the electron beam. To extract experimental cross sections using these cells the beam cur-

---

\*Corresponding Author: doug@jlab.org

rent dependent density of each target fluid must be determined. In this study, data from measurements with several beam currents within the range of 2.5 to 22.5  $\mu\text{A}$  on each target fluid are presented. Additionally, expressions for the beam dependent fluid density of each target are developed.

*Keywords:* Density, target system, tritium, helium, deuterium, hydrogen, argon

---

## 1. Introduction

A modular gas cell target system was developed for use in Hall A at Jefferson Lab for the MARATHON experiment (E12-10-103)[1]. The design was specifically developed to safely contain and operate with gaseous tritium. It is similar in luminosity and characteristics to the design purposed in Ref. [2]. The modular design allows additional gas cells filled with other species of gas to be installed in the system concurrently. The target was also adapted for the additional experiments E12-11-112 ( $x_b > 1$ ) [3], E12-14-011 ( $e'p$ ) [4], E12-17-003 (Hypernuclear) [5] and E12-14-009 (elastic) [6]. MARATHON, together with these experiments, became known as the tritium group experiments which were performed from December 2017 through November 2018. However, prior to tritium operations, a target cell was loaded with argon gas and used by the experiment E12-14-012 (Argon) [7] during Spring of 2017.

While the performance of the target was an important consideration, the primary objective of the target system design and construction was to ensure safe operations with tritium gas under all conditions. These conditions included target cell preparations, loading, storage, transportation, installation, removal, and beam operations. This was accomplished with a modular design, rigorous fabrication and testing, proper quality assurance (QA) and quality control (QC) and multiple layers of containment/confinement.

In addition to a brief description of the target, we present the beam current dependent density of the five gases used with the target system,  $^3\text{H}$ ,  $^3\text{He}$ ,  $^2\text{H}$ ,  $^1\text{H}$  and  $^{40}\text{Ar}$ . The electrons in the beam pass through the target fluid and

51 cell entrance and exit end caps depositing ionization energy. This ionization  
 52 energy, which is proportional to the beam current, induces heat in the target  
 53 fluid causing local changes in the density. To determine the magnitude of this  
 54 effect, data were collected with the Left High Resolution Spectrometer (LHRS)  
 55 in Jefferson Lab Experimental Hall A during February 2017 for the  $^{40}\text{Ar}$  target  
 56 and December 2017 for the other targets. The beam energy for the study was  
 57 2.2 GeV in all cases, The momentum and angle settings were  $17.5^\circ$  and 1.79 GeV  
 58 for  $^{40}\text{Ar}$ , and  $17.0^\circ$  and 1.99 GeV for the other fluids. Analysis of these data  
 59 shows that a simple quadratic polynomial function normalized to zero current  
 60 density provides an excellent model for all target fluids.

## 61 **2. Target System**

62 The modular design allows for multiple cell configurations. It also enables  
 63 individual cells to be installed in special configurations of the standard Hall A  
 64 Cryogenic target; this was the case for the  $^{40}\text{Ar}$  target (see Figure 1). Another  
 65 feature is that it allows cells to be filled at off site locations other than Jefferson  
 66 Lab. The tritium cell was filled at Savannah River Site (SRS) by Savannah  
 67 River Tritium Enterprises (SRTE), with about 0.1 grams of tritium gas to a  
 68 room temperature absolute pressure of about 1.38 MPa. It was shipped in a  
 69 special purpose transport container called the Bulk Tritium Shipping Package  
 70 (BTSP). Including the cell this system provided continuous triple layer confine-  
 71 ment though out the shipping and handling process. This design also allowed  
 72 the tritium cell to be placed in a special storage container in Hall A while nor-  
 73 mal Hall installation activities were completed. The tritium cell was installed  
 74 after all other preparatory tasks were completed. The modular sealed gas cell  
 75 represents a departure from previous designs [8].

76 The configuration of the target system for the tritium experiments is shown  
 77 in Figure 2. In this configuration, there are (from top to bottom) four cells  
 78 loaded with  $^3\text{H}$ ,  $^2\text{H}$ ,  $^1\text{H}$ , and  $^3\text{He}$  as well as a fifth empty cell which was used  
 79 for background measurements. The cells are contained in a scattering chamber



Figure 1: Argon cell installation. A cell filled with  $^{40}\text{Ar}$  was installed on the standard Hall A Cryogenic Target in place of the loop 3 cell.

80 which is under vacuum. The scattering chamber vacuum is isolated from the  
 81 upstream beam line vacuum by a 0.2 mm thick beryllium window. This window  
 82 is roughly 30 cm upstream of the target center and is mounted on a reentrant  
 83 tube that also contains a 15 cm long tungsten collimator with an inner diameter  
 84 of 12.7 mm. The scattering chamber vacuum, with a pumping system directed to  
 85 an exhaust stack, provided a second layer of tritium confinement. An exhaust  
 86 system, (together with strict access controls) capable of maintaining a slight  
 87 negative pressure in the experimental Hall ensured that the Hall boundary was  
 88 a third layer of confinement.

89 Each cell, excluding the fill valve assembly, is machined from ASTM B209  
 90 aluminum 7075-T651 plate. Each target cell has a cigar-tube shaped active  
 91 fluid space with a length of 25 cm and a diameter of 12.7 mm. The total  
 92 volume of the cell (including the non active region) is  $33.38 \pm 0.2 \text{ cm}^3$ . The  
 93 thickness of the nearly flat entrance window and hemispherical exit window is  
 94 nominally 0.25 mm. The parameters at the time of loading for each cell are  
 95 summarized in Table 1. Due to machining tolerances, the wall thickness of each  
 96 cell varies slightly over its length. Thickness measurements were performed for  
 97 each cell at several locations (schematically represented in Figure 3 and are



Figure 2: Ladder assembly showing the five cells,  $^3\text{H}$ ,  $^2\text{H}$ ,  $^1\text{H}$ ,  $^3\text{He}$  and empty cell from top to bottom, as assembled during Fall 2017 to Spring 2018 run period.

summarized in Table 4. The  $^{40}\text{Ar}$  cell, installed in February 2017 in a special configuration, was later evacuated and installed as the empty cell for the tritium group of experiments. Table 2 shows the  $^{40}\text{Ar}$  and the empty cell in a single column. The  $^{40}\text{Ar}$  experiment employed two aluminum foils (dummy target), with total thickness matching the radiation length of the argon filled cell, to measure backgrounds.

The entire target assembly, of five cells and assorted solid targets, was cooled with 15 K helium from the Jefferson Lab End Station Refrigerator (ESR). The 15 K helium was preheated to 40 K and used to cool a heat sink to which the cell assemblies were attached. This removed the modest amount of heat generated by the electron beam passing through the target fluid, cell entrance and cell exit, which, in total, was about 15 W. To ensure cell integrity, the maximum beam current permitted on any of the cells was  $22.5\text{ }\mu\text{A}$  [9]. The heat generated by the tritium decay is very small, about 50 mW and was negligible.

Target	Fill Pressure (kPa)	Fill Temp (K)	Thickness (mg/cm <sup>2</sup> )
$^{40}\text{Ar}$	3447	291	$1455 \pm 9.2$
$^3\text{H}$ 1 <sup>st</sup>	1400	296.3	$85.1 \pm 0.83$
$^3\text{H}$ 2 <sup>nd</sup>	1393	293.8	$84.79 \pm 0.82$
$^3\text{He}$	1772	294.3	$53.37 \pm 0.57$
$^2\text{H}$	3549	296.1	$142.15 \pm 0.80$
$^1\text{H}$	3549	297.4	$70.80 \pm 0.40$

Table 1: Load data for the gas cells. Temperatures have an uncertainty of 0.1 K. Values for the  $^{40}\text{Ar}$  cell are from Ref. [10]; for all others they are from Ref. [11].

### 3. Hall A Spectrometers

The data were acquired with the LHRS. For a detailed description of the LHRS see Ref. [13]. The basic components of the LHRS are a normal conducting quadrupole (Q1), a super conducting quadrupole (Q2) a superconducting dipole (D) followed by a super conducting quadrupole (Q3) in a Q-Q-D-Q configuration. The quadrupoles focus scattered charged particles while the dipole directs

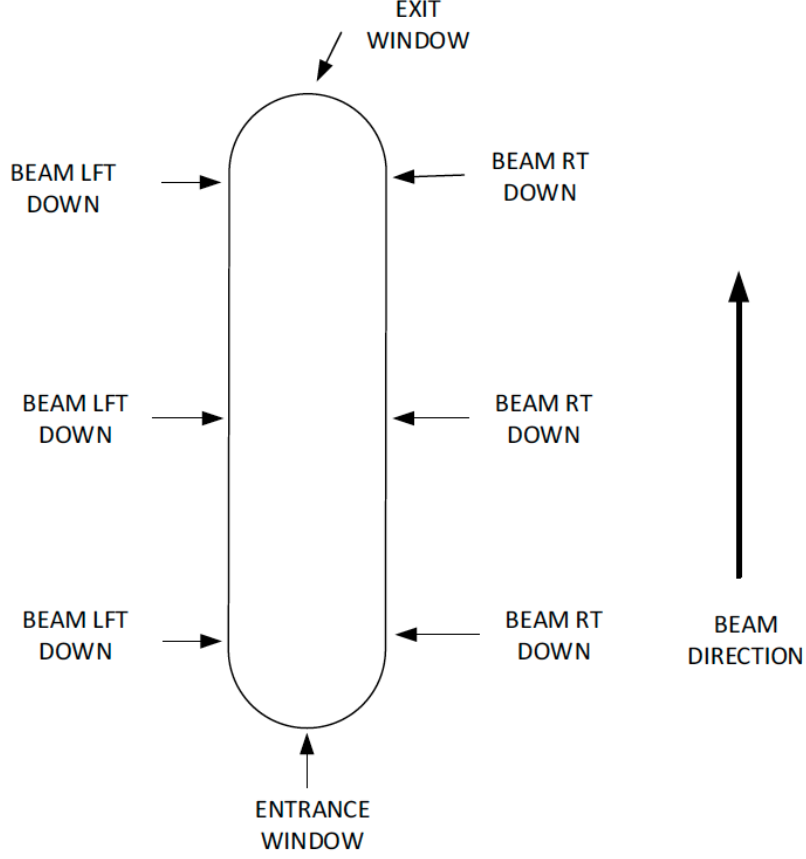


Figure 3: Measurement locations on the cells represented schematically [11].

118 these particles, within a given momentum range, to the detectors. After pass-  
 119 ing through the spectrometer magnets, the scattered particles pass through two  
 120 Vertical Drift Chambers (VDCs) that provide tracking information [14]. Two  
 121 layers of scintillator hodoscope s0 and s2, sandwich a gas Cherenkov detector  
 122 filled with CO<sub>2</sub> [15]. The hodoscope provides trigger and time of flight (TOF)  
 123 for the detected particles. The Cherenkov provides identification of electrons with  
 124 approximately 99% efficiency and reject  $\pi^-$  below momentum of 4.8 GeV. The  
 125 last element in the detector stack is the shower calorimeter. Electrons pass

Location	$^{40}\text{Ar}$ /Empty Cell Thickness (mm)	$^3\text{H}$ Cell Thickness (mm)	$^1\text{H}$ Cell Thickness (mm)	$^2\text{H}$ Cell Thickness (mm)	$^3\text{He}$ Cell Thickness (mm)
Entrance	$0.254 \pm 0.0051$	$0.253 \pm 0.004$	$0.311 \pm 0.001$	$0.215 \pm 0.004$	$0.203 \pm 0.007$
Exit	$0.279 \pm 0.0051$	$0.343 \pm 0.047$	$0.330 \pm 0.063$	$0.294 \pm 0.056$	$0.328 \pm 0.041$
Exit left	$0.406 \pm 0.0051$	$0.379 \pm 0.007$	$0.240 \pm 0.019$	$0.422 \pm 0.003$	$0.438 \pm 0.010$
Exit right	$0.421 \pm 0.0051$	$0.406 \pm 0.004$	$0.519 \pm 0.009$	$0.361 \pm 0.013$	$0.385 \pm 0.016$
Mid left	$0.457 \pm 0.0051$	$0.435 \pm 0.001$	$0.374 \pm 0.004$	$0.447 \pm 0.009$	$0.487 \pm 0.060$
Mid right	$0.432 \pm 0.0051$	$0.447 \pm 0.004$	$0.503 \pm 0.005$	$0.371 \pm 0.012$	$0.478 \pm 0.007$
Entrance left	$0.508 \pm 0.0051$	$0.473 \pm 0.003$	$0.456 \pm 0.010$	$0.442 \pm 0.005$	$0.504 \pm 0.003$
Entrance right	$0.424 \pm 0.0051$	$0.425 \pm 0.003$	$0.457 \pm 0.006$	$0.332 \pm 0.011$	$0.477 \pm 0.011$

Table 2: Cell wall thickness measurements for all gas targets. Values for the  $^{40}\text{Ar}$  cell are from Ref. [10]; for all others they are from Ref. [11].

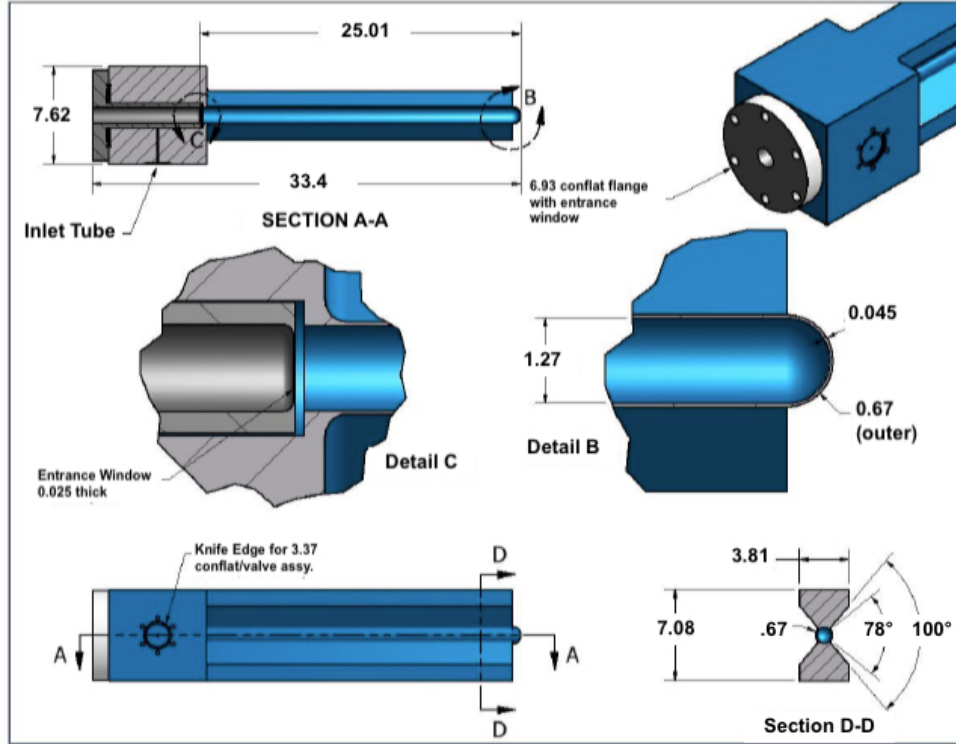


Figure 4: Engineering design of an individual tritium gas target cell [12], units are in *cm*.

126 through the calorimeter lead glass blocks induce a cascade of pair production  
127 and bremsstrahlung radiation from which their energy can be determined [13].



#### 128 4. Beam Current Monitor (BCM)

129 The Beam Current Monitor (BCM) is a system of three independent de-  
130 vices and a current source [16]. This is a dedicated system in Hall A and while  
131 independent of the target effects, this system is the dominate source of sys-  
132 tematic uncertainty in the current dependent density studies presented herein.  
133 The BCM system consists of a toroidal sensor (Unser) [17], located between an  
134 upstream and downstream RF cavity, and a data-acquisition system. A current  
135 source, which is connected to a wire which passes through the Unser, is used to  
136 calibrate the Unser immediately prior to each use of the device and the Unser  
137 is then in turn used to calibrate the BCM's with the electron beam.

138 The Unser monitor is composed of two identical toroidal cores driven in  
139 opposite ways by an external source. The DC component of the current flowing  
140 through the toroid sensor is detected by a magnetic modulator. The beam  
141 current passing through the cores produces a flux imbalance, which generates an  
142 output signal proportional to the even harmonics of the frequency of excitation,  
143 In the absence of a DC current, the sum of the signals is zero [16].

144 The temperature controlled Unser has a sensitivity to beam current of about  
145  $4 \text{ mV}/\mu\text{A}$  and has a noise canceled stability within 0.1% [16]. The system does  
146 have a DC offset which slowly drifts which typically requires the current calibra-  
147 tion to be done immediately prior to using it for an absolute current calibration  
148 of the RF cavities. Once calibrated, the RF cavities are used to continuously  
149 monitor the beam current. The calibrations are checked periodically through  
150 out the course of an experiment. To put the signals from the Unser and RF  
151 cavities into the scalers of Hall's fast data aquition system, a voltage to fre-  
152 quency (V/F) converter is used along with a discriminator. Figure 5 shows the  
153 Unser calibration with a known DC current source, the response of the system  
154 is found to be  $(249.7 \pm 9.6) \times 10^{-6} \mu\text{A}/\text{Hz}$ .

155 Two resonant cavities surround the Unser and are tuned to the frequency of  
156 the beam 1.497 GHz. The cavities are composed of loop antennas located where  
157 the magnetic field is maximum. When the beam passes through, the output RF

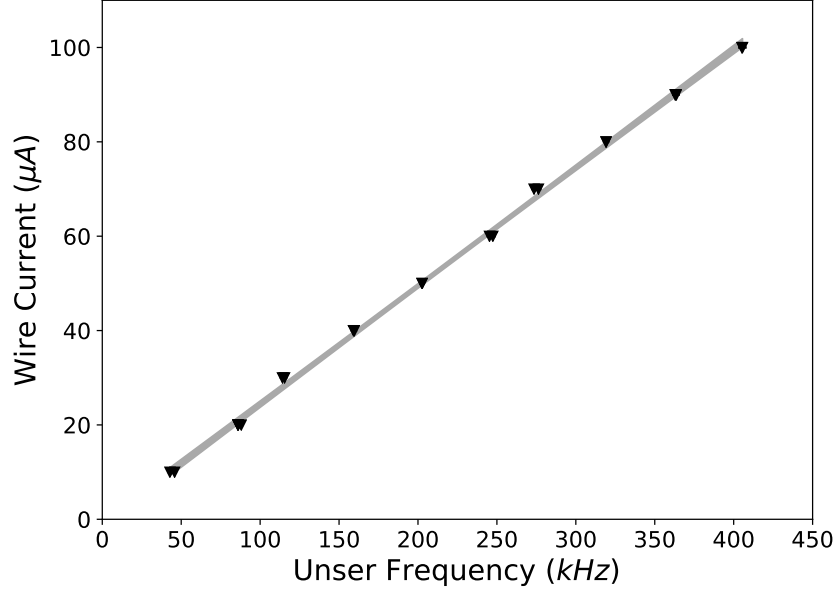


Figure 5: Wire Unser calibration. The band represents the 95% confidence level of the linear fit.

158 signal is proportional to the current [16]. As consequence, the BCM response is  
 159 linear with respect to the current. Like the Unser, the signals from the RF cav-  
 160 ities are filtered by a V/F converter. Several values of beam current (measured  
 161 by the calibrated Unser) are used to the determine the linear dependence of the  
 162 BCM as shown in Fig. 6. In general, the beam current can be then calculated  
 163 using

$$I = g_{\text{BCM}} \cdot f + O. \quad (1)$$

164 where  $g_{\text{BCM}}$  and  $O$  are the fit parameters, which correspond to  $(326.4 \pm 1.4) \times$   
 165  $10^{-6} \mu\text{A}/\text{Hz}$  and  $0.1 \pm 0.09 \mu\text{A}$ , respectively. Finally, for any given beam induced  
 166 frequency  $f$ , the current  $I$  is given by Eq 1. Of unfortunate note, the BCM  
 167 system becomes much less accurate for beam currents below  $\sim 5 \mu\text{A}$ .

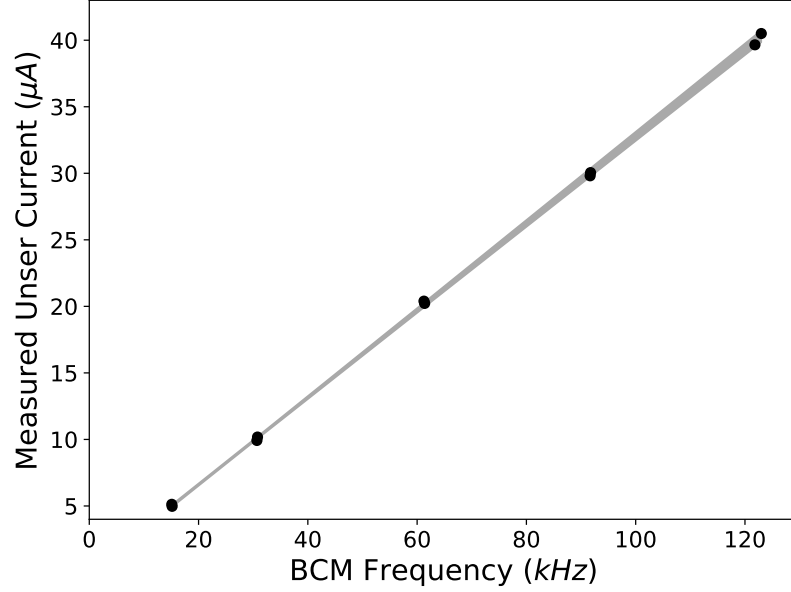


Figure 6: BCM calibration. The band represents the 95% confidence level of the linear fit.

## 168 5. Method Overview

169 The density of the target is well known when loaded but, experience and  
 170 simulations have shown that the beam current will decrease the density of the  
 171 target fluid in the beam path (local density). The magnitude of this effect de-  
 172 pends on the beam current and target fluid species and must be quantified to  
 173 accurately determine cross sections and ratios or other comparisons of data col-  
 174 lected with the multiple gas cells [12]. It was shown (with the exception of the  
 175 argon cell) that the target density reaches equilibrium within an insignificant  
 176 amount of time from when the electron beam first impinges on the cell and  
 177 the density was constant with stable beam current. The purpose of these mea-  
 178 surements and analysis is to develop a beam current dependent target density  
 179 function for each gas species used.

180 In order to extract the current dependent density correction the raw yield

181 is measured for several beam currents. The normalized yield is determined by  
 182 applications of corrections to the raw yield. These corrections include: total  
 183 charge, particle identification, acceptance cuts, detector efficiencies, and live  
 184 times. The normalized yield  $Y_{\text{norm}}$  is then given by

$$Y_{\text{norm}} = \frac{PS \cdot N}{Q \cdot \epsilon \cdot LT} \quad (2)$$

185 Where  $N$  is the number of good electrons,  $PS$  is the prescale factor of the DAQ  
 186 system,  $Q$  is the total charge, and  $\epsilon$  is the combined efficiencies of detectors,  
 187 triggers and events selection cuts and  $LT$  is the live-time. Each one of these  
 188 parameters is explained in detail in the following sections.

### 189 5.1. Event Selection

190 To improve counting efficiency and minimize dead time, a compound trigger  
 191 was used. This trigger required both scintillator planes and the Cherenkov  
 192 detector to have signals above threshold, in order to exclude  $\pi^-$  events. In  
 193 order to extract a good electron sample, several cuts were applied to the data.  
 194 These cuts can be summarized in two groups: acceptance cuts, which assure  
 195 that the events are selected within an acceptable spectrometer phase space,  
 196 and tracking/particle iDentification (PID) Cuts, which focus on the selection of  
 197 electrons scattered from the target fluid. These selection cuts are:

- 198 i. Momentum and angular acceptance cuts. Specifically, the ranges used to  
 199 determine  $Y_{\text{norm}}$  are  $|\delta p/p| < 4.5\%$ ,  $|\theta - \theta_0| < 30$  mrad and  $|\phi| < 25$  mrad.
- 200 ii. Target length cut. This cut excluded events reconstructed back to the  
 201 target windows and reduced background by limiting the effective target  
 202 length  $|y_{\text{tar}}| < 8$  cm
- 203 iii. Only events with a single track in the VDC were kept.
- 204 iv. A particle ID cut was applied to the Cherenkov ADC sum
- 205 v. A particle ID cut was applied to the shower calorimeter

206 It was shown through the course of this study that as long as the sample of  
 207 electrons is chosen consistently, the results will remain invariant within 1% run  
 208 to run.

## 209 *5.2. Estimation of Efficiencies*

210 A number of efficiencies were applied to the data to produce  $Y_{\text{norm}}$ . For  
 211 simplicity, in this analysis only electron events with one track in the VDC were  
 212 selected. The ratio between the total number of electron events with one track  
 213 with respect to the total number of triggered electrons (including multi track  
 214 and non track particles) corresponds to the VDC efficiency.

215 The trigger efficiency was calculated using another trigger type, where only  
 216 both scintillators were required to record the events. In this sense, the difference  
 217 between the main trigger and the efficiency trigger is the Cherenkov detector.  
 218 The ratio between the events recorded with the main and the efficiency trigger  
 219 corresponds to the trigger efficiency.

220 The Cherenkov efficiency was calculated by selecting a clean sample of elec-  
 221 trons detected in the Calorimeter and counting the number of events that also  
 222 were detected in the Cherenkov detector. The Calorimeter efficiency was mea-  
 223 sured by selecting a clean sample of electrons in the Cherenkov detector and  
 224 counting the number of these electrons that also fired the Calorimeter.

## 225 *5.3. Live-Time Calculation*

226 The live-time is related with the limitation of the speed of data acquisition  
 227 system (DAQ) to record events. It depends on the electronics, computers and  
 228 trigger rate and is calculated using the ratio between the number of events  
 229 recorded over the total number of events seen by the trigger.

## 230 *5.4. Total Charge*

231 The beam is not completely stable throughout the run; it may trip off or  
 232 fluctuate over time. Therefore, we obtained the calibration data when the beam  
 233 was mostly stable, and only runs where the average current is within a window of

234  $\pm 2 \mu\text{A}$  of the requested current are used. The charge is calculated by integrating  
 235 the current over time using the BCM calibration result (see Section 4).

## 236 6. Solid Target Check

237 The aim of the analysis is to measure the density change when the beam is  
 238 on the gas targets using the Yield analysis. In order to test the method, the  
 239 same analysis is applied to a solid target. For the  $^{40}\text{Ar}$  experiment, a carbon  
 240 foil was used, and for the Tritium experiments an aluminum target. Unlike the  
 241 fluid targets, the solid target density is not measurably effected by the beam  
 242 current.

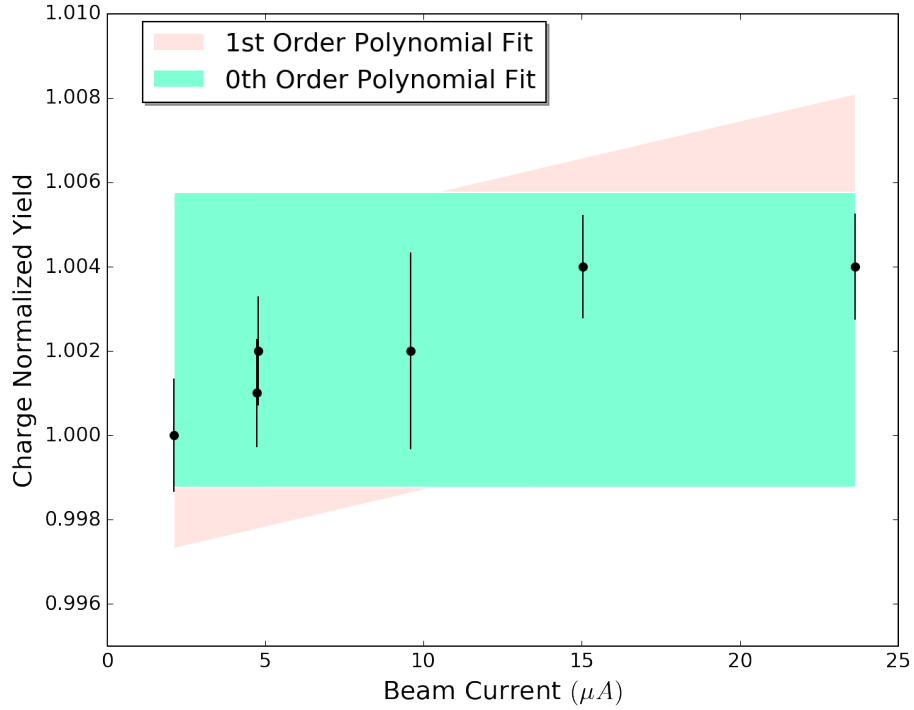


Figure 7: Normalized Yield analysis for the aluminum solid target used during the tritium group experiments

243 Figure 7 shows  $Y_{\text{norm}}$  for the solid aluminum target which was calculated  
 244 using Equation 2 for different beam currents. It was normalized with respect

245 to the lowest current Yield value. The plot shows that  $Y_{\text{norm}}$  did not change to  
 246 within about 0.5% which is well within the uncertainty of the measurement.

## 247 **7. Background Contamination**

248 The aluminum windows of the target cell contribute as background to the  
 249 measured raw yield for each of the gas targets. To measure this background  
 250 (henceforth referred to as contamination) in the case of the  $^{40}\text{Ar}$  experiment, a  
 251 dummy target with aluminum foils with total thickness matching the radiation  
 252 length of the argon filled cell, was used. In the case of the tritium experiments,  
 253 an empty cell (or dummy cell) was used. The normalized yields from these  
 254 targets were then subtracted from the applicable  $Y_{\text{norm}}$ . To check the current  
 255 dependence of this subtraction, a comparison between the background at low  
 256 and high current was measured for the dummy/empty targets. The charge yield  
 257 given by Eq 1 was binned in  $y_{\text{tar}}$  bites along the target length, and the ratio of  
 258 the events at high current to low current was determined. The ratio was found  
 259 to be 1.006, which indicates that the background subtraction is independent of  
 260 current, as expected.

261 Figure 8 shows the spectra of the charge normalized yield for the empty  
 262 (dummy) cell and the tritium gas, for a beam current of  $2.5 \mu\text{A}$ . To optimize  
 263 the signal to background ratio, events contributing to the  $Y_{\text{norm}}$  were selected  
 264 from a symmetric region of  $\pm 8 \text{ cm}$  about the center of the target. Therefore,  
 265 the contamination fraction is the ratio of  $Y_{\text{norm}}$  for the empty cell to  $Y_{\text{norm}}$   
 266 for the gas cell of interest. Table 3 summarizes the percentage of background  
 267 contamination found in the gas targets for each beam current used in the study.  
 268 Note that the currents are nominal; the measured current for each run is slightly  
 269 different, due to the normal operation of the accelerator.

## 270 **8. Gas Target Results**

271 The density correction was determined for each gas species by measuring  
 272  $Y_{\text{norm}}$  as a function of beam current  $I_{\text{beam}}$ . The function is then normalized

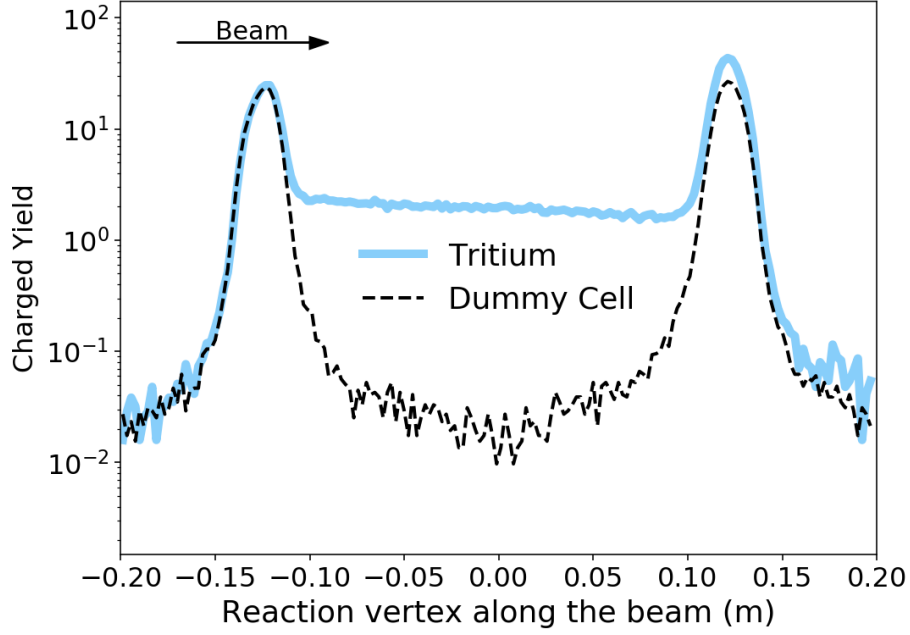


Figure 8: Background contamination spectrum of the dummy target compared with that of tritium at 2.5  $\mu\text{A}$ . Both spectra are normalized.

Current ( $\mu\text{A}$ )	$^3\text{H}$ (%)	$^3\text{He}$ (%)	$^2\text{H}$ (%)	$^1\text{H}$ (%)	Current ( $\mu\text{A}$ )	Argon (%)
2.5	1.7	1.6	0.7	1.1	2.5	0.3
5	1.7	1.6	0.7	1.2	4.5	0.3
10	1.7	1.7	0.8	1.2	8	0.3
15	1.8	1.8	0.8	1.3	12	0.3
22.5	1.8	1.8	0.8	1.3	15	0.3
					18	0.3

Table 3: Aluminum window contamination in a  $\pm 8\text{ cm}$  range with respect to the center of the target at each nominal current. Note that these currents were not the same for both experiments.

273 to 1 for  $I_{\text{beam}} = 0$ . The density each gas cell for zero beam current is the  
274 same as that of the load density. Figures 9, 10a, 10b, 10c and 10d, show the



275 density correction for the different gas targets. It is easily seen that the density  
 276 decreases with the current and that the behavior of the density correction factor  
 277  $f$  is modeled well by a quadratic function

$$f(I_{\text{beam}}) = a \cdot I_{\text{beam}}^2 + b \cdot I_{\text{beam}} + c. \quad (3)$$

278 Where  $a$ ,  $b$  and  $c$  are the fit parameters. Table 4 shows the fit parameters for  
 279 each gas species. The density correction factor  $f(I_{\text{beam}})$  is determined for each  
 280 gas by substitution of these parameters in Eq 3. The density correction factor  
 281 determined in this manner is valid for the current range  $0 - 22.5 \mu A$ . The  
 282 error bar in the plots represents the statistical uncertainty only, and a fit was  
 283 calculated with respect to those values with a 95% confidence band in blue. The  
 284 gray hatched 95% confidence band represents a fit including both statistical and  
 285 systematic uncertainties.

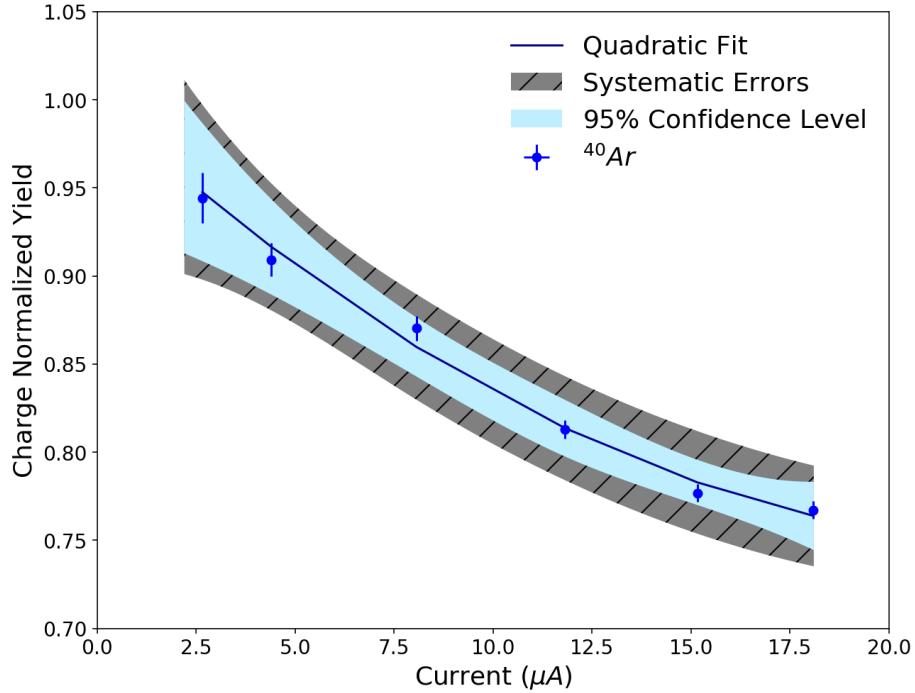


Figure 9:  $^{40}\text{Ar}$  density analysis.

<b><math>^3\text{H}</math> Fit Parameters</b>		<b><math>^3\text{H}</math> Correlation Factors</b>	
<b>a</b>	$(1.06 \pm 0.36) \times 10^{-4}$	<b>C(a, b)</b>	-0.974
<b>b</b>	$(-6.8 \pm 0.89) \times 10^{-3}$	<b>C(b, c)</b>	-0.888
<b>c</b>	$1. + / - 0.003$	<b>C(a, c)</b>	0.801
<b><math>^3\text{He}</math> Fit Parameters</b>		<b><math>^3\text{He}</math> Correlation Factors</b>	
<b>a</b>	$(1.04 \pm 0.25) \times 10^{-4}$	<b>C(a, b)</b>	-0.973
<b>b</b>	$(-5.1 \pm 0.64) \times 10^{-3}$	<b>C(b, c)</b>	-0.879
<b>c</b>	$1 \pm 0.003$	<b>C(a, c)</b>	0.779
<b><math>^2\text{H}</math> Fit Parameters</b>		<b><math>^2\text{H}</math> Correlation Factors</b>	
<b>a</b>	$(1.16 \pm 0.29) \times 10^{-4}$	<b>C(a, b)</b>	-0.973
<b>b</b>	$(-6.7 \pm 0.71) \times 10^{-3}$	<b>C(b, c)</b>	-0.895
<b>c</b>	$1. \pm 0.003$	<b>C(a, c)</b>	0.805
<b><math>^1\text{H}</math> Fit Parameters</b>		<b><math>^1\text{H}</math> Correlation Factors</b>	
<b>a</b>	$(1.70 \pm 0.47) \times 10^{-4}$	<b>C(a, b)</b>	-0.978
<b>b</b>	$(-9 \pm 0.12) \times 10^{-3}$	<b>C(b, c)</b>	-0.881
<b>c</b>	$1. \pm 0.006$	<b>C(a, c)</b>	0.788
<b><math>^{40}\text{Ar}</math> Fit Parameters</b>		<b><math>^{40}\text{Ar}</math> Correlation Factors</b>	
<b>a</b>	$(4.33 \pm 1.5) \times 10^{-4}$	<b>C(a, b)</b>	-0.981
<b>b</b>	$(-2.1 \pm 0.3) \times 10^{-2}$	<b>C(b, c)</b>	-0.942
<b>c</b>	$1. \pm 0.02$	<b>C(a, c)</b>	0.867

Table 4: Fit parameters obtained for the percentage of density change calculation with respect to the beam current.

### 8.1. Systematic Uncertainties

Several corrections are applied to the data in this analysis. and since the current is different for every point, the uncertainties are evaluated at every point. A confidence band for a fit including the systematic uncertainties are shown in Figures 9, 10a, 10b, 10c and 10d. they include the uncertainty in the charge, live-time and detectors calculations.

The BCM monitors are effective over a range from 0 to 100  $\mu\text{A}$ . However, low

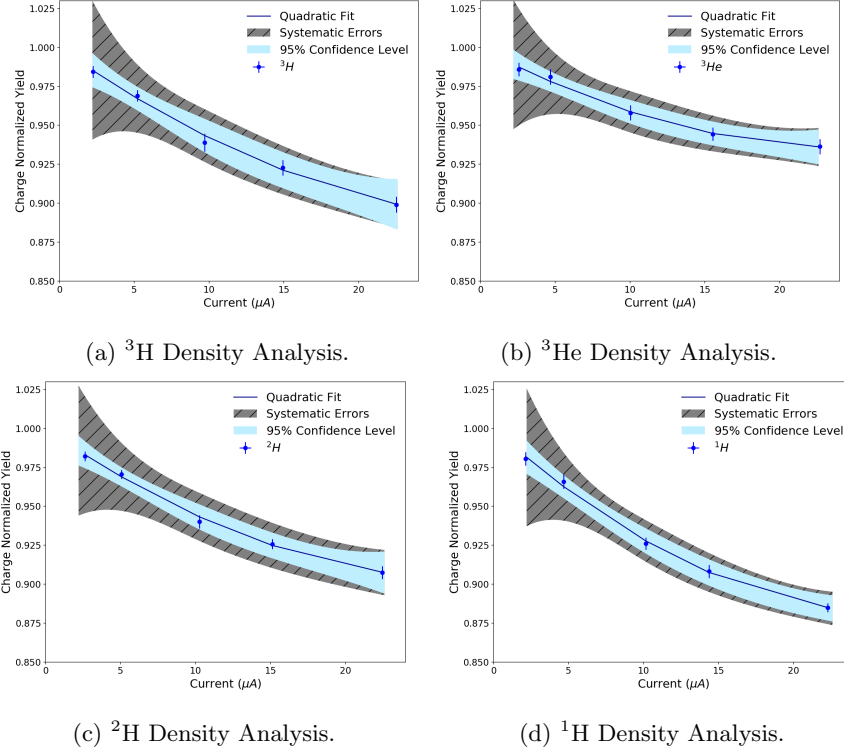


Figure 10: Density analysis of  $^3\text{H}$ ,  $^3\text{He}$ ,  $^2\text{H}$  and  $^1\text{H}$ .

current measurements have a slightly higher uncertainty causing the uncertainty in the charge to be current dependent. The uncertainty in the current and charge is estimated using the BCM calibration shown in Figure 6, together with the error covariance matrix. This is the dominant source of systematic uncertainty in the determination of the density reduction factor  $f(I_{\text{beam}})$ .

The background contamination coming from the entrance and exit windows also contribute as a source of systematic uncertainty. This is due to the thickness variations in the cell entrance and exit windows which can be seen in Figure 8. Therefore, in order to calculate the background uncertainty in the measurement, the percentage of background was calculated in  $y_{\text{tar}}$  steps of 3 cm starting from  $\pm 4$  cm out to  $\pm 10$  cm from the center of the target. The same normalization procedure was followed for each of the different cuts in the reaction vertex region

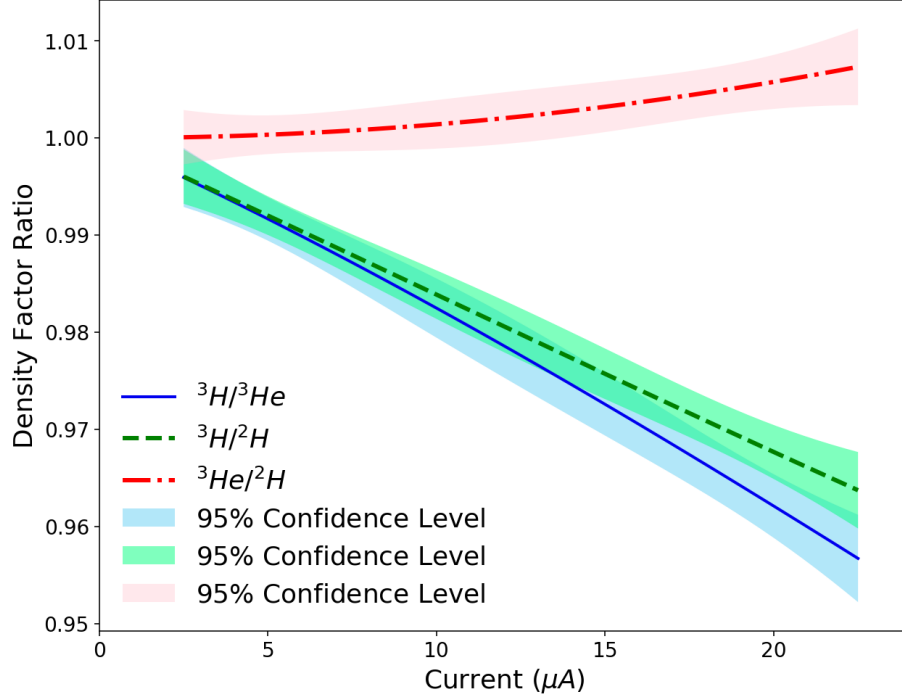


Figure 11: Density Factor Ratios.

305 to calculate  $f(I_{\text{beam}})$ . Finally, the uncertainty in the background contamination  
 306 is given by the standard deviation of the average of multiple  $f(I_{\text{beam}})$  obtained  
 307 with the different cuts. The standard deviation was never more than 1% for  
 308 each current.

309 Furthermore, 1% systematic uncertainties were estimated for the live-time,  
 310 VDC One-Track efficiency, trigger efficiency, detector and cut efficiencies of Gas  
 311 Cerenkov and  $\pi^-$  rejection.

## 312 8.2. Conclusions

313 Current dependent density correction functions have been determined for  
 314 several species of gas target cells. The maximum density change for each target  
 315 is  $9.7 \pm 0.5\%$ ,  $5.6 \pm 0.5\%$ ,  $6.3 \pm 0.5\%$ ,  $11.6 \pm 0.5\%$  and  $26.5 \pm 1\%$  for  $^3\text{H}$ ,  $^3\text{He}$ ,  
 316  $^2\text{H}$ ,  $^1\text{H}$  and  $^{40}\text{Ar}$ , respectively at  $22.5 \mu\text{A}$ .

## 317 9. Acknowledgments

318 We wish to thank the staff of the Thomas Jefferson National Accelerator  
319 Facility especially the accelerator staff and Hall A and target group techni-  
320 cal staffs. We also acknowledge the critical efforts of Savannah River Site and  
321 Savannah River Tritium Enterprises. This work was supported by the U.S.  
322 Department of Energy (DOE) contract DE-AC05-06OR23177 under which Jef-  
323 ferson Science Associates operates the Thomas Jefferson National Accelerator  
324 Facility, DOE contract DE-AC02-06CH11357 and by National Science Founda-  
325 tion (NSF) Grant No. NSF PHY 1506459.

- 326 [1] G. Petratos, et al., JLab Experiment E12-10-103 (2010).
- 327 [2] B. Brajuskovic, T. O'Connor, R. J. Holt, J. Reneker, D. Meekin, P. Solvi-  
328 gnon, Thermomechanical design of a static gas target for electron ac-  
329 celerators, Nucl. Instrum. Meth. A729 (2013) 469–473. arXiv:1306.6000,  
330 doi:10.1016/j.nima.2013.06.090.
- 331 [3] P. Solvignon, et al., JLab Experiment E12-11-112 (2011).
- 332 [4] O. Hen, L. B. Weinstein, S. Gilad, W. Boeglin, et al., JLab Experiment  
333 E12-14-011 (2013).
- 334 [5] L. Tang, F. Garibaldi, P. E. C. Markowitz, S. N. Nakamura, J. Reinhold,  
335 G. M. Urciuoli, JLab Experiment E12-17-003 (2017).
- 336 [6] L. S. Myers, D. W. Higinbotham, J. R. Arrington, JLab Experiment E12-  
337 14-009 (2014). arXiv:1408.5283.
- 338 [7] O. Benhar, et al., JLab Experiment E12-14-012 (2014). arXiv:1406.4080.
- 339 [8] D. Beck, et al., A Cryogenic tritium target system for nuclear physics ex-  
340 periments, Nucl. Instrum. Meth. A277 (1989) 323–337. doi:10.1016/0168-  
341 9002(89)90761-4.
- 342 [9] D. Meekins, Hall A Tritium Target TGT-RPT-17-003, Jefferson Lab Engi-  
343 neering Report.

- 344 [10] D. Meekins, Hall A Argon Target Configuration (2017).
- 345 [11] D. Meekins, Hall A Tritium Target Configuration TGT-PRT-17-007, Jef-  
346 ferson Lab Engineering Report.
- 347 [12] R. Holt, W. Korsch, D. Meekins, T. O. Connor, G. Petratos, R. Ransome,  
348 P. Solvignon, B. Wojtsekhowski, A Tritium Gas Target for Jefferson Lab  
349 (2015).
- 350 [13] J. Alcorn, et al., Basic Instrumentation for Hall A at Jefferson Lab, Nucl.  
351 Instrum. Meth. A522 (2004) 294–346. doi:10.1016/j.nima.2003.11.415.
- 352 [14] K. G. Fissum, et al., Vertical drift chambers for the Hall A high-resolution  
353 spectrometers at Jefferson Lab, Nucl. Instrum. Meth. A474 (2001) 108–131.  
354 doi:10.1016/S0168-9002(01)00875-0.
- 355 [15] M. Iodice, et al., The CO-2 gas Cherenkov detectors for the Jefferson  
356 Lab Hall-A spectrometers, Nucl. Instrum. Meth. A411 (1998) 223–237.  
357 doi:10.1016/S0168-9002(98)00235-6.
- 358 [16] J. Denard, A. Saha, G. Lavessiere, High Accuracy Beam Current Monitor  
359 System for CEBAF’s Experimental Hall A, Conf. Proc. C0106181 (2001)  
360 2326–2328, [,2326(2001)].
- 361 [17] K. B. Unser, The Parametric current transformer: A Beam current  
362 monitor developed for LEP, AIP Conf. Proc. 252 (1992) 266–275.  
363 doi:10.1063/1.42124.